INTERNATIONAL JOURNAL FOR NUMERICAL METHODS IN FLUIDS, VOL. 17, 177–193 (1993)

A KINETIC THEORY SOLUTION METHOD FOR THE NAVIER–STOKES EQUATIONS

M. N. MACROSSAN AND R. I. OLIVER

Department of Mechanical Engineering, University of Queensland, St Lucia, Qld 4072, Australia

SUMMARY

The kinetic-theory-based solution methods for the Euler equations proposed by Pullin and Reitz are here extended to provide new finite volume numerical methods for the solution of the unsteady Navier–Stokes equations. Two approaches have been taken. In the first, the equilibrium interface method (EIM), the forward- and backward-flowing molecular fluxes between two cells are assumed to come into kinetic equilibrium at the interface between the cells. Once the resulting equilibrium states at all cell interfaces are known, the evaluation of the Navier–Stokes fluxes is straightforward. In the second method, standard kinetic theory is used to evaluate the artificial dissipation terms which appear in Pullin's Euler solver. These terms are subtracted from the fluxes and the Navier–Stokes dissipative fluxes are added in. The new methods have been tested in a 1D steady flow to yield a solution for the interior structure of a shock wave and in a 2D unsteady boundary layer flow. The 1D solutions are shown to be remarkably accurate for cell sizes large compared to the length scale of the gradients in the flow and to converge to the exact solutions as the cell size is decreased. The steady-state solutions obtained with EIM agree with those of other methods, yet require a considerably reduced computational effort.

KEY WORDS Viscous flow Kinetic theory Finite volume method

1. INTRODUCTION

Pullin[1] and Reitz[2] proposed numerical methods for the solution of the Euler equations which exploited the fact that these equations can be derived from the Boltzmann equation of the kinetic theory of gases in the limit of an infinite molecular collision rate. These kinetic theory methods are automatically upwinding in the sense that they ensure that information is transmitted in the physically correct directions. Deshpande[3] has called these methods 'kinetic flux vector splitting methods'. Pullin's method, which he called the Equilibrium Flux Method, or EFM, is a finite volume method more conveniently applied to multidimensional flows[4–6] than Reitz's method. It is the purpose of this paper to develop Pullin's finite volume kinetic theory method into a solution method for the Navier–Stokes equations.

In one dimension Pullin's method can be shown to be equivalent to a finite difference method for the solution of the Euler equations with added pseudo-dissipative terms which are strong functions of the local Mach number.[4] In general, a finite volume shock-capturing method for solving the Euler equations usually solves, in effect, an equation similar to the Navier–Stokes equations in integral form (see equation (1)). That is, an Euler solver produces fluxes which are estimates of the Euler fluxes $\mathbf{F}_E$, yet contain something which can be interpreted as inherent numerical or artificial dissipation. The size of this dissipation may vary from point to point in the computational grid. Such a method can be converted to a method for the Navier–Stokes

0271–2091/93/150177–17$13.50

Received April 1992
Revised January 1993

equations by adding the appropriate dissipative flux terms to the flux expressions, but this is futile if the inherent dissipation of the Euler method is so large as to overwhelm the true dissipation term. EFM can be made second-order accurate[7] by the standard *min-mod* gradient strategy[8,9] and could be the basis of a Navier–Stokes solver. A different approach is to eliminate the inherent dissipation in the first-order version of EFM before adding the Navier–Stokes fluxes. Another kinetic theory approach, also described below, does not quite eliminate the pseudo-dissipation terms of the underlying Euler solver before the correct dissipative fluxes are added.

2. THE NAVIER–STOKES EQUATIONS

Consider a space (x, y, z) divided into N contiguous elements of volume V_j for $j=1, N$. Let S be the surface of V_j and $\hat{\mathbf{n}}$ the outward normal, and let the unit vectors $\hat{\mathbf{p}}$ and $\hat{\mathbf{q}}$ form with $\hat{\mathbf{n}}$ an orthogonal set of local axes at the surface S. Let $\mathbf{v}$ be the local fluid velocity and let (v_n, v_p, v_q) denote its components relative to the local axes. The Navier–Stokes equations for the conservation of mass, momentum and energy in integral or control volume form can be written for each volume V_j as

$$\frac{\partial}{\partial t}\int_{V_j} \mathbf{U}\,\mathrm{d}V + \int_S (\mathbf{F}_\mathrm{E}+\mathbf{F}_\mathrm{D})\,\mathrm{d}S = 0, \tag{1}$$

where the conserved quantities (per unit volume) are

$$\mathbf{U}=\begin{bmatrix} \rho \\ \rho v_n \\ \rho v_p \\ \rho v_q \\ \rho(\frac{1}{2}\mathbf{v}^2+e_{\mathrm{int}}) \end{bmatrix}, \tag{2}$$

and the fluxes across S are written in two parts: the *Euler* fluxes

$$\mathbf{F}_\mathrm{E}=\begin{bmatrix} \rho v_n \\ \rho v_n v_n+\rho RT \\ \rho v_n v_p \\ \rho v_n v_q \\ \rho v_n[\frac{1}{2}\mathbf{v}^2+\gamma RT/(\gamma-1)] \end{bmatrix}, \tag{3}$$

and the *dissipative* fluxes

$$\mathbf{F}_\mathrm{D}=-\begin{bmatrix} 0 \\ \tau_{nn} \\ \tau_{np} \\ \tau_{nq} \\ (v_n\tau_{nn}+v_p\tau_{np}+v_q\tau_{nq})-q_n \end{bmatrix}. \tag{4}$$

In equation (2), e_{int} is the specific internal energy and a perfect gas equation of state, $p=\rho RT=\rho(\gamma-1)e_{\mathrm{int}}$, where R is the ordinary gas constant, has been assumed. The τ_{nj} are the stresses (excluding the thermodynamic pressure) acting on the surface S and q_n is the component

of the heat flux vector normal to S. These are related to the strain rates in the fluid by the constitutive relations

$$\tau_{nn}=(4\mu/3+\mu_B)\partial v_n/\partial x_n+(\mu_B-2\mu/3)(\partial v_p/\partial x_p+\partial v_q/\partial x_q), \tag{5}$$

$$\tau_{np}=\mu(\partial v_n/\partial x_p+\partial v_p/\partial x_n), \tag{6}$$

$$\tau_{nq}=\mu(\partial v_n/\partial x_q+\partial v_q/\partial x_n), \tag{7}$$

and

$$q_n=-k\,\partial T/\partial x_n, \tag{8}$$

where μ is the coefficient of dynamic viscosity, μ_B is the coefficient of bulk viscosity, k is the thermal conductivity and (x_n, x_p, x_q) are position co-ordinates measured in the directions of the unit vectors $\hat{\mathbf{n}}$, $\hat{\mathbf{p}}$ and $\hat{\mathbf{q}}$ attached to the surface S.

3. KINETIC THEORY SOLUTION METHODS FOR THE CONTINUUM EQUATIONS

The Boltzmann equation is the fundamental equation of the kinetic theory of gases and can be written as

$$\partial(\mathrm{nf})/\partial t+\mathbf{c}\cdot\nabla(\mathrm{nf})=D_c(\mathrm{nf}), \tag{9}$$

where n is the number density of the molecules of the gas, $f(\mathbf{c}, \varepsilon_{st}, \mathbf{x}, t)$ is the molecular velocity distribution function, $\mathbf{x}$ is the position, $\mathbf{c}$ is the molecular velocity and ε_{st} is the energy in the molecular structure (i.e. rotational, vibrational, electronic energy, etc.) divided by the mass of the molecule m. The right-hand side of (9) represents the collision integral.[10] The conservation equations which are solved by EFM can be derived by first multiplying (9) by the molecular quantities $Q=[m, m\mathbf{c}, m(\frac{1}{2}\mathbf{c}^2+\varepsilon_{st})]$. The resulting equation is then integrated over V_j and over all molecular velocities $\mathbf{c}$ and over all ε_{st}. The resulting term on the RHS,

$$\int_0^\infty\int_{V_j}\int_{-\infty}^{\infty} QD_c(\mathrm{nf})\,\mathrm{d}\mathbf{c}\,dV\,\mathrm{d}\varepsilon_{st},$$

is a source term giving the production of Q by collisions and it vanishes since the sum of Q over the collision partners is conserved for each collision. After applying the divergence theorem to the second volume integral on the LHS, we have

$$\frac{\partial}{\partial t}\int_{V_j}\mathbf{U}\,\mathrm{d}V+\int_S\mathbf{F}\,\mathrm{d}S=0, \tag{10}$$

where

$$\mathbf{U}=\int_0^\infty\int_{-\infty}^{\infty} nQf\,\mathrm{d}\mathbf{c}\,\mathrm{d}\varepsilon_{st} \tag{11}$$

and

$$\mathbf{F}=\int_0^\infty\int_{-\infty}^{\infty} nQf\mathbf{c}\cdot\hat{\mathbf{n}}\,\mathrm{d}\mathbf{c}\,\mathrm{d}\varepsilon_{st}. \tag{12}$$

From (11) the components of $\mathbf{U}$ can be evaluated and are, for any nf,

$$[\rho, \rho\mathbf{v}, \rho(\tfrac{1}{2}\mathbf{v}^2+e_{int})],$$

where $\rho = mn$, $\mathbf{v} = \int f \mathbf{c}\, d\mathbf{c}$ is the mean molecular velocity or macroscopic fluid velocity, $e_{\text{int}} = \int_0^\infty \int_{-\infty}^\infty (\frac{1}{2}\vartheta^2 + \varepsilon_{\text{st}}) f \, d\mathbf{c}\, d\varepsilon_{\text{st}}$ and $\vartheta = \mathbf{c} - \mathbf{v}$ is the random or thermal part of the molecular velocity. In other words $\mathbf{U}$ is the same as $\mathbf{U}$ in (2) except that e_{int} is a more general quantity than the corresponding thermodynamic state variable which is strictly defined for a state of thermodynamic equilibrium only.

It is a standard result of kinetic theory that the Navier–Stokes equations can be obtained from (10) if the distribution function which appears in (12) is the Chapman–Enskog distribution, which is of the form[10]

$$nf = nf_0(1 + \Phi), \tag{13}$$

where

$$nf_0 = n(\beta^3/\pi^{3/2}) \exp[-\beta^2(\mathbf{c} - \mathbf{v})^2](RT)^{-1} \exp[-\varepsilon_{\text{st}}/RT], \tag{14}$$

$\beta = (2RT)^{-1/2}$, and T is the temperature given by $(\gamma - 1)e_{\text{int}}/R$. This distribution is a small perturbation about the local Maxwell–Boltzmann equilibrium distribution nf_0 and the perturbation Φ is related to the gradients of macroscopic flow properties. It is also a standard result that in the limit $f \to f_0$ the fluxes in (12) reduce to the Euler fluxes $\mathbf{F}_{\text{E}}$ in (3).

The first approach taken here to evaluate the dissipative fluxes for a finite volume scheme is to derive first the local-equilibrium distribution function, $n_0 f_0$, at the interface S between two cells. Then the distribution function at S could be found from (13) provided that the local gradients $\partial v_i/\partial x_j$ and $\partial T/\partial x_j$ at the interface are known. Putting this distribution into (12) would produce the appropriate kinetic theory Navier–Stokes fluxes. The same result may be obtained more easily since, if $n_0 f_0$ is known, the state $\mathbf{U}_s$ at the interface between two cells is also known and the Euler part of the fluxes can be evaluated from (3). Furthermore, if the flow gradients are known, the dissipative fluxes can be found directly from (5)–(8). Viewed in this way, the proposed method may be thought of as a kinetic theory alternative to methods[8,11] which determine the interface state by solving a Riemann problem. We propose that this kinetic theory method be called the 'equilibrium interface method' or EIM.

4. THE EQUILIBRIUM INTERFACE METHOD

Assuming local equilibrium within each cell adjacent to the surface S and a step change at S yields, for the molecules crossing S, the non-equilibrium distribution function

$$n_S f_S = \begin{cases} n^+ f_0^+, & c_n > 0, \\ n^- f_0^-, & c_n < 0, \end{cases} \tag{15}$$

where c_n is the component of molecular velocity normal to the surface and the $+$ and $-$ superscripts refer to the flow conditions interior and exterior to V_j, respectively. The distribution is split into two parts since molecules on S having $c_n > 0$ have come from inside V_j while those having $c_n < 0$ have come from outside V_j.

The equilibrium distribution function at S is then assumed to be that distribution which would be brought about by the action of collisions amongst an isolated group of molecules which initially conformed to the distribution (15). Since the total mass, momentum and energy of the isolated group of molecules remain unchanged by collisions, the state corresponding to the

equilibrium distribution $n_0 f_0$ on the interface surface S is given by the condition that

$$\iint Q n_0 f_0 \, \mathrm{d}\mathbf{c} \, \mathrm{d}\varepsilon_{\mathrm{st}} = \iint Q n_S f_S \, \mathrm{d}\mathbf{c} \, \mathrm{d}\varepsilon_{\mathrm{st}}$$
$$= \int_0^\infty \int_{-\infty}^\infty \int_{-\infty}^\infty \int_0^\infty Q n^+ f_0^+ \, dc_n \, dc_p \, dc_q \, d\varepsilon_{\mathrm{st}}$$
$$+ \int_0^\infty \int_{-\infty}^\infty \int_{-\infty}^\infty \int_{-\infty}^0 Q n^- f_0^- \, dc_n \, dc_p \, dc_q \, d\varepsilon_{\mathrm{st}}. \tag{16}$$

The interface density $\rho_0 = m n_0$ is found by putting $Q = m$ in (16) to get

$$\rho_0 = W^+ \rho^+ + W^- \rho^-, \tag{17}$$

where the weighting factor $W^\pm$ is given by

$$W^\pm = [1 \pm \mathrm{erf}(s_n^\pm)]/2 \tag{18}$$

and

$$s_n^\pm = v_n^\pm \beta^\pm. \tag{19}$$

Putting $Q = mc_n$, mc_p and mc_q in (16) yields the three components of the interface velocity $\mathbf{v}_0$:

$$v_{n0} = (W^+ \rho^+ v_n^+ + W^- \rho^- v_n^-)/\rho_0 + (D^+ \rho^+ / \beta^+ + D^- \rho^- / \beta^-)/\rho_0, \tag{20}$$

$$v_{p0} = (W^+ \rho^+ v_p^+ + W^- \rho^- v_p^-)/\rho_0, \tag{21}$$

$$v_{q0} = (W^+ \rho^+ v_q^+ + W^- \rho^- v_q^-)/\rho_0, \tag{22}$$

where

$$D^\pm = \pm \exp[-(s_n^\pm)^2]/(2\pi^{1/2}). \tag{23}$$

Finally, putting $Q = m(\frac{1}{2}\mathbf{c}^2 + \varepsilon_{\mathrm{st}})$ in (16), we get

$$\tfrac{1}{2}\mathbf{v}_0^2 + e_{\mathrm{int}\,0} = [W^+ \rho^+ (\tfrac{1}{2} v^+ v^+ + e_{\mathrm{int}}^+) + W^- P^- (\tfrac{1}{2} v^- v^- + e_{\mathrm{int}}^-)]/\rho_0$$
$$+ (D^+ \rho^+ v_n^+ / \beta^+ + D^- \rho^- v_n^- / \beta^-)/2\rho_0. \tag{24}$$

The interface temperature can then be determined as

$$T_0 = (\gamma - 1) e_{\mathrm{int}\,0} / R. \tag{25}$$

The Euler fluxes, $\mathbf{F}_{\mathrm{EO}}$, corresponding to this equilibrium interface state are obtained by putting $\rho = \rho_0$, $\mathbf{v} = \mathbf{v}_0$ and $T = T_0$ in (3) and the dissipative fluxes are obtained directly from (4)–(8).

5. A NAVIER–STOKES SOLVER—METHOD II

Another approach appears at first glance to be the same but is subtly different. First the fluxes are evaluated by assuming that the distribution function on S is given by (15). These are, in fact, the EFM fluxes derived by Pullin.[1] Next the viscous stresses and heat flux vector for this distribution are evaluated. These quantities, which are denoted by $\mathbf{F}^{\mathrm{D}}$, make up the inherent dissipative part of the EFM fluxes. These dissipative fluxes are subtracted from the EFM fluxes and the dissipative

fluxes of (4)–(8) are added in. Thus, this second numerical method solves, in effect, the equation

$$\frac{\partial}{\partial t}\int_{V_j}\mathbf{U}\,\mathrm{d}V+\int_S(\mathbf{F}-\mathbf{F}^{\mathrm{D}}+\mathbf{F}_{\mathrm{D}})\,\mathrm{d}S=0, \tag{26}$$

where $\mathbf{F}-\mathbf{F}^{\mathrm{D}}$ is an approximation to the Euler part of the fluxes.

The components of $\mathbf{F}^{\mathrm{D}}$ can be evaluated by the standard procedure in kinetic theory. First, the pressure tensor

$$p_{ij}=\int_{-\infty}^{\infty}\int_{-\infty}^{\infty}\int_{-\infty}^{\infty}\vartheta_i\vartheta_j m n_S f_S\,\mathrm{d}c_n\,\mathrm{d}c_p\,\mathrm{d}c_q. \tag{27}$$

is evaluated, where $n_S f_S$ is given by (15). In (27) $\vartheta=\mathbf{c}-\mathbf{v}_0$ is the thermal velocity relative to the mean velocity $\mathbf{v}_0$ given by (20)–(22). The viscous stresses in $\mathbf{F}^{\mathrm{D}}$ are given by

$$\tau_{nn}=-(p_{nn}-p'),$$

$$\tau_{np}=-p_{np},$$

$$\tau_{nq}=-p_{nq},$$

where the non-equilibrium pressure p' is given by $(p_{nn}+p_{pp}+p_{qq})/3$ and p_{pp} and p_{qq} can be evaluated from (27). The results are[12]

$$\tau_{nj}=\tau_{nj}^{+}+\tau_{nj}^{-}, \tag{28}$$

where

$$\tau_{nn}^{\pm}=W^{\pm}\rho^{\pm}\{(\mathbf{v}^{\pm}-\mathbf{v}_0)^2-2(v_{n0}-v_n^{\pm})^2\}/3+2D^{\pm}\rho^{\pm}(2v_{n0}-v_n^{\pm})/3\beta^{\pm}, \tag{29}$$

$$\tau_{np}^{\pm}=W^{\pm}\rho^{\pm}(v_n^{\pm}-v_{p0})(v_{p0}-v_p^{\pm})+D^{\pm}\rho^{\pm}(v_{p0}-v_p^{\pm})/\beta^{\pm}, \tag{30}$$

$$\tau_{nq}^{\pm}=W^{\pm}\rho^{\pm}(v_n^{\pm}-v_{q0})(v_{q0}-v_q^{\pm})+D^{\pm}\rho^{\pm}(v_{q0}-v_q^{\pm})/\beta^{\pm}, \tag{31}$$

The thermal energy flux across the surface in the direction of $\hat{\mathbf{n}}$ for the distribution $n_S f_S$ is given from kinetic theory as

$$\phi_n=\int_0^{\infty}\int_{-\infty}^{\infty}[\vartheta_n(\vartheta_n\vartheta_n+\vartheta_p\vartheta_p+\vartheta_q\vartheta_q)/2+\vartheta_n\varepsilon_{\mathrm{st}}]\,m n_S f_S\,\mathrm{d}\mathbf{c}\,\mathrm{d}\varepsilon_{\mathrm{st}}, \tag{32}$$

which, with $n_S f_S$ given by (15), can be split as

$$\phi_n=\phi_n^{+}+\phi_n^{-}. \tag{33}$$

The split components of ϕ_n are[12]

$$\begin{aligned}\phi_n^{\pm}=&W^{\pm}\rho^{\pm}[\tfrac{1}{2}(\mathbf{v}^{\pm}-\mathbf{v}_0)^2+\tfrac{1}{4}(7\gamma-5)RT^{\pm}/(\gamma-1)](v_n^{\pm}-v_{n0})\\&+(D^{\pm}\rho^{\pm}/\beta^{\pm})[\tfrac{1}{2}(\mathbf{v}^{\pm}-\mathbf{v}_0)^2+v_{n0}^2-\tfrac{1}{2}v_n^{\pm}v_{n0}+\tfrac{1}{4}(5\gamma-3)RT^{\pm}/(\gamma-1)].\end{aligned} \tag{34}$$

The total outward energy flux term in $\mathbf{F}^{\mathrm{D}}$ includes the flux of the mean translational energy as well as the thermal energy and is

$$-(v_{n0}\tau_{nn}+v_{p0}\tau_{np}+v_{q0}\tau_{nq}-\phi_n), \tag{35}$$

where $\mathbf{v}_0$ is given by (20)–(22) and the τ_{ij} are given by (28)–(31). The component corresponding to $Q=m$ in $\mathbf{F}^{\mathrm{D}}$ is zero.

The fluxes $\mathbf{F}-\mathbf{F}^{\mathrm{D}}$, in the second method, differ from the fluxes $\mathbf{F}_{\mathrm{E0}}$ of the equilibrium interface method primarily because the translational and structural parts of the molecular energy are not

brought into equilibrium with each other. Consequently, the approximation to the Euler fluxes, $\mathbf{F}-\mathbf{F}^{D}$ does not correspond exactly to any equilibrium distribution function.

6. 1D TEST CASE: SHOCK WAVE INTERNAL STRUCTURE

As a first test of these new methods, each has been used to obtain a numerical solution of the Navier–Stokes equations for the one-dimensional flow through a plane normal shock wave. These solutions are compared with the numerical solution obtained by integrating the continuum Navier–Stokes equations, following the method of Gilbarg and Paolucci,[13] which is referred to hereafter as the 'exact solution'.

Figure 1 shows a typical exact solution for the density profile through a plane shock wave in the frame of reference in which the shock is stationary. Upstream flow conditions are denoted by the subscript 1 and downstream values by the subscript 2. The solution asymptotes to the upstream and downstream values, which are related by the Rankine–Hugoniot relations. The origin of the x-axis is at the point where $\rho=(\rho_1+\rho_2)/2$. A convenient length scale is the upstream mean free path evaluated as

$$\lambda_1 = 1{\cdot}25\,\frac{\mu_1}{\rho_1(RT_1)^{1/2}}. \tag{36}$$

The gas was assumed to have a constant ratio of specific heats of $\gamma=1{\cdot}4$. The viscosity and thermal conductivity were given by the Sutherland formulae

$$\mu=\mu_0(T/T_0)^{3/2}(T_0+S_v)/(T+S_v), \tag{37}$$

and

$$k=k_0(T/T_0)^{3/2}(T_0+S_k)/(T+S_k), \tag{38}$$

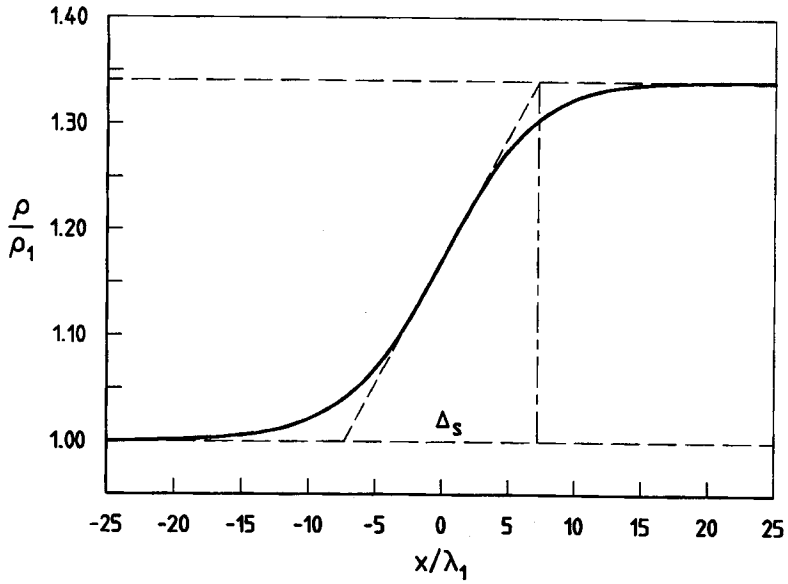

Figure 1. A typical density profile through a plane shock. The shock thickness Δ_s is obtained from the maximum density gradient inside the shock

with the following constants which are appropriate for nitrogen: $\mu_0 = 16{\cdot}63 \times 10^{-6}\ \mathrm{N\,m^{-2}\,s}$, $k_0 = 0{\cdot}02423\ \mathrm{W\,m^{-1}\,K^{-1}}$, $T_0 = 273{\cdot}15\ \mathrm{K}$, $S_v = 106{\cdot}7\ K$ and $S_k = 166{\cdot}7\ \mathrm{K}$. The bulk viscosity for nitrogen has been taken[14] as $7\mu/15$. The pre-shock conditions were $T_1 = 223\ \mathrm{K}$ and $\rho_1 = 0{\cdot}41\ \mathrm{kg\,m^{-3}}$.

In the finite volume methods the discretized version of (1) was advanced by the explicit time-stepping scheme

$$\left[\int_{V_j} \mathbf{U}\,\mathrm{d}V\right]_{t+\mathrm{d}t} = \left[\int_{V_j} \mathbf{U}\,\mathrm{d}V\right]_t - \left[\int_S (\mathbf{F_E} + \mathbf{F_D})\,\mathrm{d}S\right]_t \mathrm{d}t, \tag{39}$$

where $\mathbf{F_E}$ represents the estimation of the Euler fluxes associated with each method. In one dimension, the surface integral in (39) can be divided into contributions from two faces in each cell, and the flow was assumed to have reached steady state when the surface integral divided by the maximum of the contribution from the two faces was less than 10^{-5} in every cell. A one-dimensional regular grid was used, and the $\partial(*)/\partial n$ derivatives in (5) and (8) were evaluated by central differences.

The initial conditions for the shock problem were given by a step function between the appropriate upstream and downstream values of all flow properties. This discontinuity gradually relaxed into a steady smooth profile between the fixed boundary cells located at $x \cong \pm 30\lambda_1$. The first test was for $M = 1{\cdot}2$ and cell sizes were $0{\cdot}5 \leqslant \Delta x/\lambda_1 \leqslant 9$. The results for the smallest cell size are compared with the exact solution in Figure 2. Also shown is a solution obtained by the naive method (denoted as Method III) of adding the appropriate Navier–Stokes terms to the flux expressions for first-order EFM. As expected, the inherent dissipation in first-order EFM makes this approach the least accurate. In contrast, the solution for EIM is extremely accurate at this cell size and slightly better than Method II.

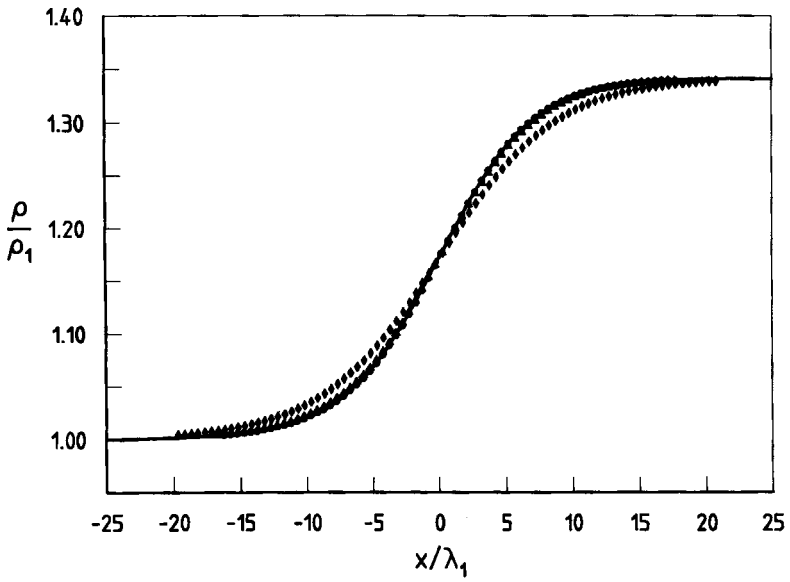

Figure 2. Density profiles in a plane shock with $M_s = 1{\cdot}2$ calculated by: ● EIM; ▲ Method II; ◆ Method III; —— exact solution of Reference 13

A measure of the accuracy of these numerical solutions is given by the shock thickness Δ_s (see Figure 1) determined from the maximum density gradient within the shock, that is,

$$\Delta_s = (\rho_2 - \rho_1)/(\partial\rho/\partial x)_{\max}.$$

The shock thicknesses determined for the three methods on different grids are shown in Figure 3. Each method is converging to the exact value as a linear function of Δx (first-order

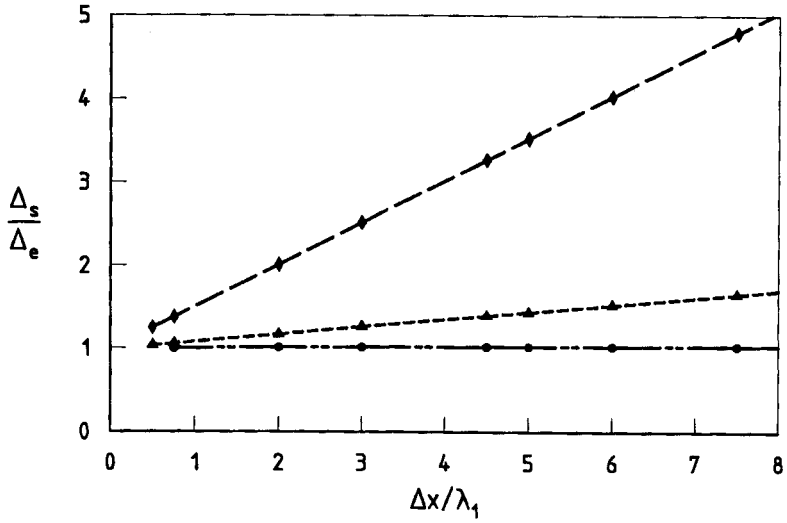

Figure 3. Shock thickness Δ_s (for $M_s = 1{\cdot}2$) as calculated by the three kinetic theory methods compared with the exact shock thickness Δ_e. See Figure 2 for legend. All methods converge to the exact solution as $\Delta x \to 0$

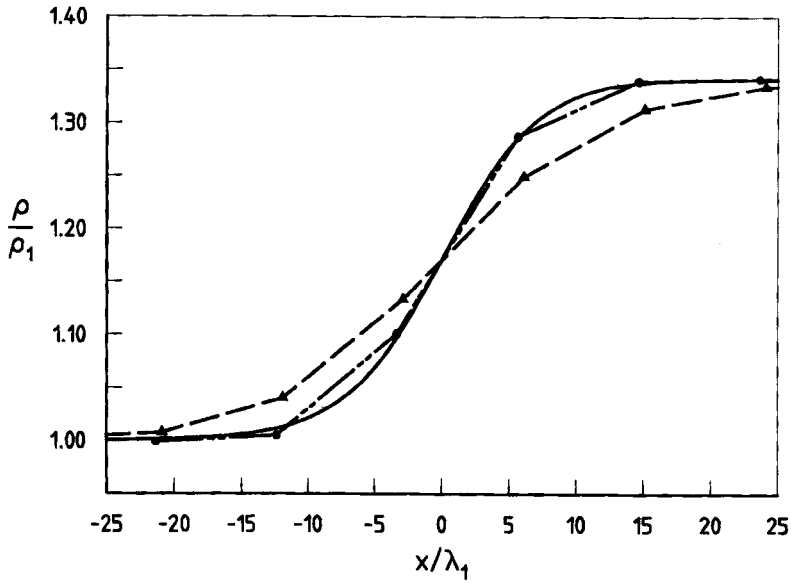

Figure 4. Density profiles in a plane shock ($M_s = 1{\cdot}2$) for a cell size $\Delta x = 9\lambda_1$, calculated by: ---●--- EIM; —▲— Method II; ——exact solution of Reference 13

convergence). Note, however, that the EIM results are always very close to the exact solution even for cell sizes large compared to the characteristic length scale (λ_1) of the shock structure being resolved. The shock profiles calculated with a large cell size, $\Delta x = 9\lambda_1$, are shown in Figure 4, and the results for EIM are remarkably accurate.

Calculations were made for shock Mach numbers of $M_s = 3$, 6 and 9, for which the exact values of Δ_s were found to be $2{\cdot}31\lambda_1$, $1{\cdot}87\lambda_1$ and $1{\cdot}81\lambda_1$, respectively. EIM was unstable for cell sizes greater than $3\lambda_1$ for all these Mach numbers while Method II was stable for cell sizes up to $15\lambda_1$ in all cases. This indicates that the most accurate method (EIM) as it stands may not generally be shock capturing on the grids that are normally used in aerospace work, where the cell size may be orders of magnitude larger than the correct shock thickness. This is discussed further in Section 8.

7. 2D TEST CASE: UNSTEADY DEVELOPMENT OF A BOUNDARY LAYER

The new methods were used to calculate the unsteady development of a boundary layer on a flat plate. The flow chosen was the same as the one chosen by Jacobs[15] to test his finite volume Navier–Stokes code. Jacobs' code seems representative of those currently in use. The dissipative fluxes have been added to a second-order-accurate (in space) inviscid flow solver[16] in which the inviscid fluxes are determined by solving a one-dimensional Riemann problem at each interface between cells. The states on either side of the interface before the application of the Reimann solver are dertermined by assuming gradients of flow properties across the cells.

Jacobs considered a perfect gas with a ratio of specific heats of $\gamma = 1{\cdot}4$ and with viscosity given by a Sutherland viscosity law (37) with a constant $S_v = 110{\cdot}4$ K. The bulk viscosity was taken as zero and the thermal conducitivity was taken as proportional to the vicosity with a constant Prandtl number of 0·72. The body was a flat plate aligned with the freestream velocity. The freestream Mach number and temperature were, respectively $M_1 = 2$ and $T_1 = 222$ K. The wall temperature was fixed at $T_w = T_1$. The Reynolds number, $Re_L = \rho_1 U_1 L/\mu_1$, based on the free-stream conditions and the plate length L was $1{\cdot}65 \times 10^5$. Jacobs has also used a spectral method[17] to solve the standard boundary layer equations (derived from the Navier–Stokes equations by dropping a number of terms) and has made that solution, as well as the results from his finite volume code, available to us for comparison.

A schematic diagram of the grid used in our calculations is shown in Figure 5. The cell boundaries are parallel to the x- or y-axis and the cell dimensions Δx and Δy vary in an arithmetic progression, with the smallest Δy closest to the plate and the smallest Δx near the upstream (west) boundary of the grid. The grid was extended to $x = L$ and $y = 0{\cdot}68L$, and the upper (north) boundary was held at the freestream conditions. The fluxes at the downstream (east) boundary were determined by assuming that there were no gradients of any properties in the x-direction at this boundary. The unsteady development of the flow from an impulsive start was calculated with a CFL number of 0·8 which is same as that used by Jacobs.[15]

The Euler components of the fluxes at the wall were calculated by using a ghost cell below the wall and using the general algorithm at the wall. The only property in the ghost cell which differs from the corresponding property in the adjacent cell within the flow is the velocity normal to the wall, which is reversed. This ensures that the mass, parallel momentum and energy components of the Euler fluxes at the wall are zero. After the Euler fluxes at each interface are calculated, the dissipative fluxes $\mathbf{F}_D$ of (4)–(8) are added in.

The flow gradients which appear in (5), (6) and (8) were evaluated at each cell interface using a quadratic fit to three values of the flow state. The central value is always the value for the equilibrium interface state, determined when calculating the inviscid fluxes, and the other two values are, for gradients normal to the interface, the adjacent cell centred states or, for gradients

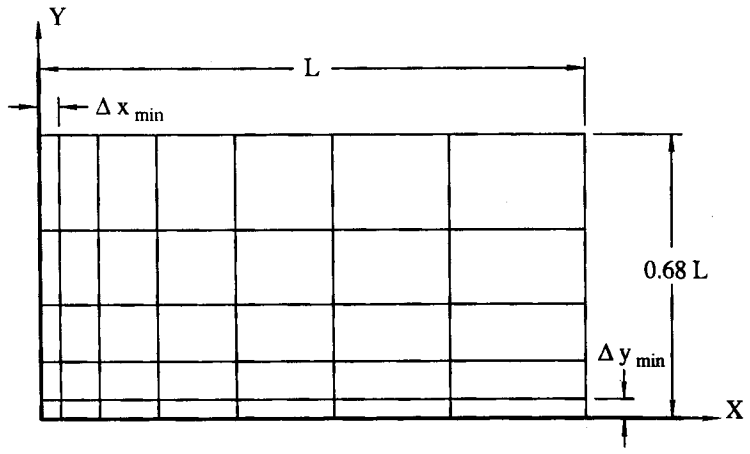

Figure 5. A schematic diagram of a typical finite volume grid used for the flat plate problem. All cells are rectangular and the cell side lengths vary in an arithmetic progression in the x- and y-direction. The boundary at $y=0$ is a wall at a fixed temperature

parallel to the interface, the adjacent interface states. At the wall, the fluid velocity was taken as zero and the temperature was taken as the known wall temperature. Gradients at the plate surface, normal to the surface, were determined by fitting a quadratic to the known values of velocity and temperature at the wall and the values at the centre of the first two cells out from the wall in the y-direction.

Figure 6 shows the pressure contours as calculated with EIM at two values of time elapsed since the impulsive start of the flow. For the larger elapsed time the flow is very nearly steady. The weak leading-edge interaction shock has been captured and it is reasonably clear that the north and east boundaries should have little effect on the results in the boundary layer.

The development of the boundary layer as calculated by EIM can be seen in Figure 7, which shows the x-component of velocity at the station $x/L=0{\cdot}916$ at different times after the impulsive start of the flow. The two kinetic theory methods were found to give very similar velocity profiles but, as shown in Figure 8(a), rather different temperature profiles. It is shown below that EIM agrees with other methods for this flow, and this, coupled with the results obtained for the 1D flow in Section 6, indicates that EIM is considerably more accurate than the second method. This difference should be reduced for a gas in which no internal energy is stored in the molecular structure. Results were obtained for the two methods for a flow with the same freestream Mach number but with $\gamma=5/3$ and all other properties as given above. In this case the temperature profiles in the boundary layer were indistinguishable, as shown in Figure 8(b). The second method is not considered further here.

Different grids were used to show that the EIM solutions near the rear of the plate (at $x/L=0{\cdot}916$) are independent of the cell size. The temperature profiles in the boundary layer for these grids are shown in Figure 9 and the details regarding the grids are given in Table I. Only two of the grids gave results easily distinguishable from those on the more refined grids, but the differences were very small.

Figure 10 shows a comparison of the temperature profile across the boundary layer for EIM on a 52×250 grid with the spectral solution and the finite volume solution given by Jacobs[15] on a 50×50 grid. At this station (near the rear of the plate), the cell sizes in the boundary layer are similar for the two finite volume methods, but near the front of the plate, where the boundary

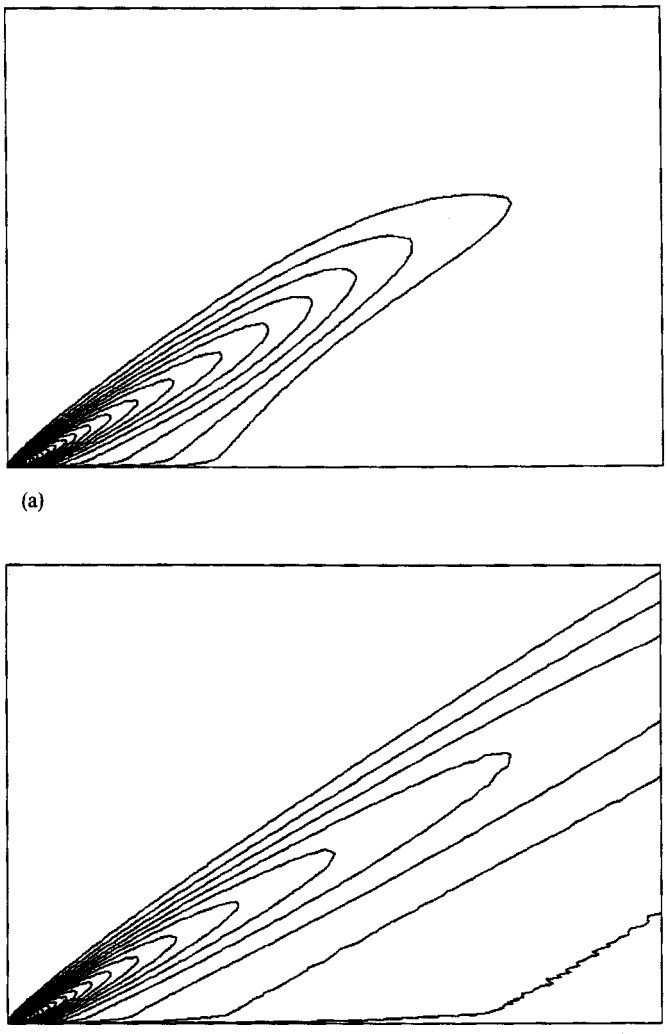

Figure 6. Pressure contours $p/p_1 = 1{\cdot}01, 1{\cdot}015, 1{\cdot}02, \ldots$ calculated by EIM on grid 1, Table I. $M_1 = 2{\cdot}0$, $Re_L = 1.65 \times 10^5$, $\gamma = 1{\cdot}4$, $Pr = 0{\cdot}7$, $T_1 = T_w = 222$ K, with viscosity given by (37) and a Sutherland constant $S_v = 110{\cdot}4$ K. Grid 1, Table I. (a) $tU_1/L = 0{\cdot}96$ (b) $tU_1/L = 4{\cdot}78$

layer develops, Jacobs has used cells which are very much smaller in both dimensions than the cells in our grid. His grid is not orthogonal and extends in the y-direction little further than the edge of the leading-edge interaction shock.

Both finite volume solutions agree with the spectral solution near the wall and past the point of maximum temperature but differ slightly from the spectral solution near the edge of the boundary layer. Note that the boundary conditions imposed on the spectral solution of the boundary layer equations at the edge of the boundary layer are identical to the freestream conditions. In fact, however, these conditions should be slightly different from the freestream conditions because of the weak leading-edge interaction shock. This is probably enough to account for the difference in

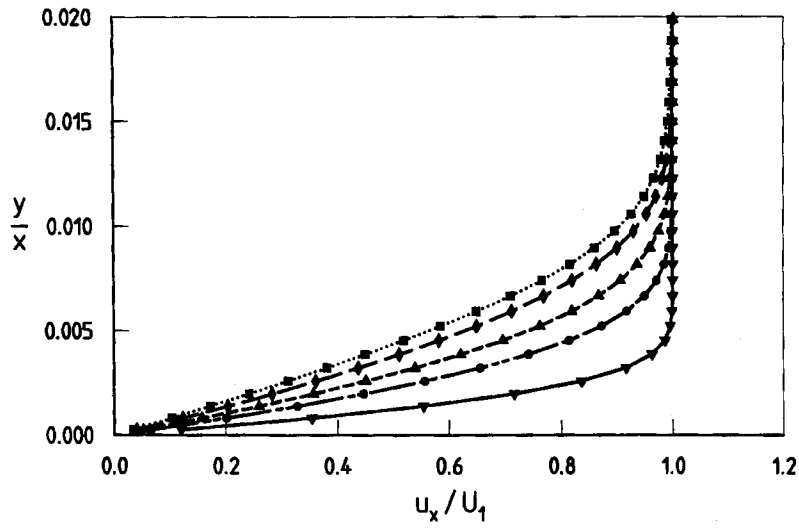

Figure 7. Unsteady development of the boundary layer. x-velocity profile for EIM at $tU_1/L = 0{\cdot}19$, $0{\cdot}66$, $1{\cdot}10$, $1{\cdot}91$ and $4{\cdot}78$. Conditions as for Figure 6. Grid 2, Table I

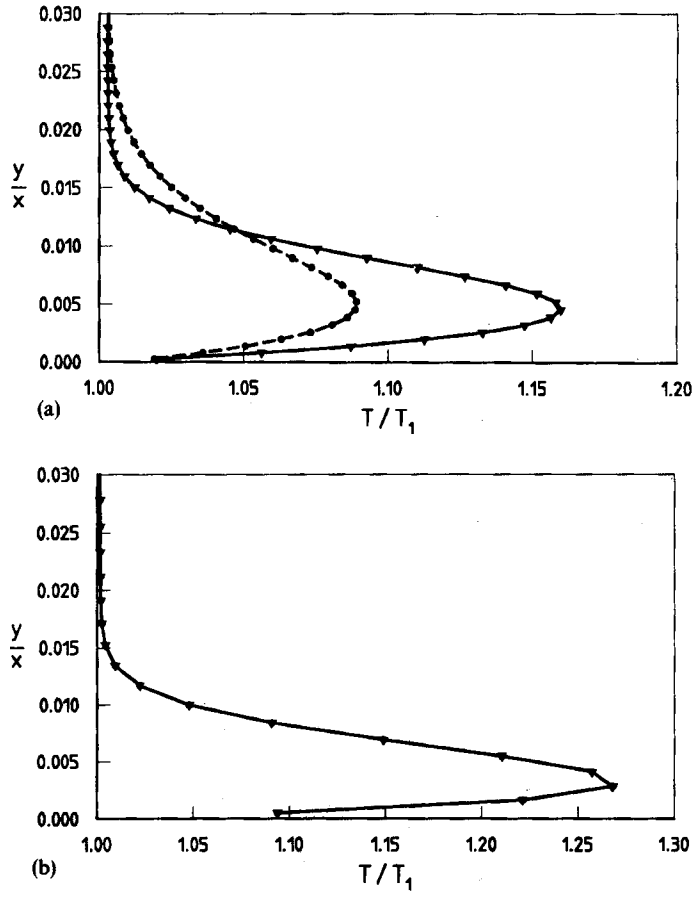

Figure 8. Kinetic theory methods compared: —▼— EIM; —●— Method II. (a) for conditions as in Figure 6, $\gamma = 1{\cdot}4$, $tU_1/L = 4{\cdot}78$. (b) $\gamma = 5/3$, $tU_1/L = 1{\cdot}0$

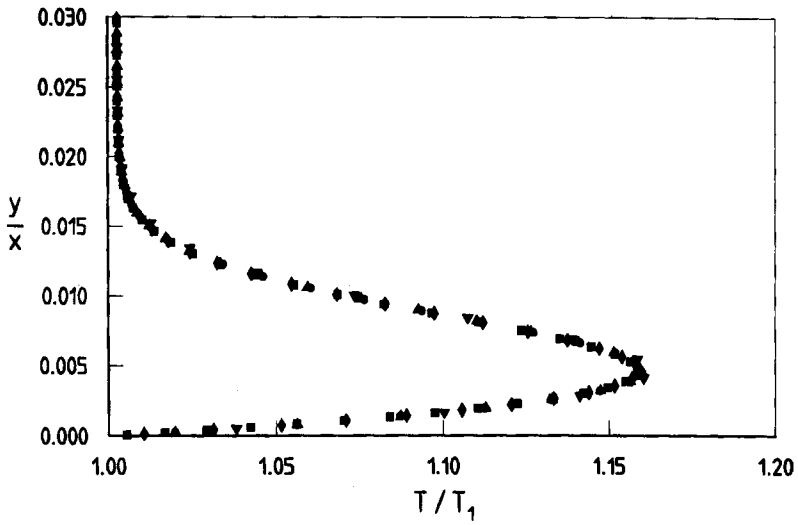

Figure 9. Temperature profiles at $x/L=0{\cdot}916$ on different grids (EIM): ▼ Grid 1, ● grid 2, ▲ grid 3, ◆ grid 4, ■ grid 5. Conditions as in Figure 6

Table I.

	Grid size $N_x \times N_y$	$\Delta x/L$	$\Delta y/L$[a] (10^{-4})	Number of time steps	Total CPU[b] (h)	Effective Y-MP time[c] (μs/cell/time step)
1	52 × 125	35·1	9·89	4200	2·74[e]	12·0
2	52 × 250	35·0	4·95	8338	2·81[f]	11·6
3	52 × 250	18·4	4·95	8475	11·0[e]	12·0
4	52 × 250	35·0	2·59	15 760	20·0[e]	11·8
5	52 × 250	35·0	1·33	29 108	27·8[g]	—

[a] Shows the smallest cell dimension in each direction. Cell dimensions increased in an arithmetic progression in the positive x- and y-direction. The relative size of largest to smallest cell is different in different calculations.
[b] Values marked [e] are for a Sun Microsystems SPARC station 2. The value marked [f] is for an IBM RISC/6000 530 workstation, while the value marked [g] is for the same machine without the optimizing switches set on the xlf compiler.
[c] Shows the estimated time/cell/time step on a single processor of a Cray Y-MP, calculated assuming that a SPARC 2 and an IBM 530 are equivalent to 1/30 and 1/8 of a Cray, respectively.

All calculations were advanced until a simulated time of $tU_1/L \cong 4{\cdot}78$. The time-step was varied slightly throughout the calculation to keep the CFL number in any cell to $\leqslant 0{\cdot}8$.

the profiles shown in Figure 10, since the temperature calculated by the finite volume methods is slightly greater than freestream temperature and is falling very slowly with increasing distance from the plate.

Figure 11 shows the EIM result for the velocity profile at $x/L=0{\cdot}916$ compared with the spectral solution of the boundary layer equations and with Jacobs' solution. Here we show the results for our coarsest grid, for which the temperature profile is very little different from that shown in Figure 10. Once again, the agreement with the other methods is good.

Tabe I shows the CPU time required to obtain the nearly steady flow over the flat plate for different grids and the estimated Cray Y-MP CPU time for the kinetic theory method. The estimated 'Cray time' of about 12 μs/cell/timestep is about half of that reported by Jacobs.[15] For

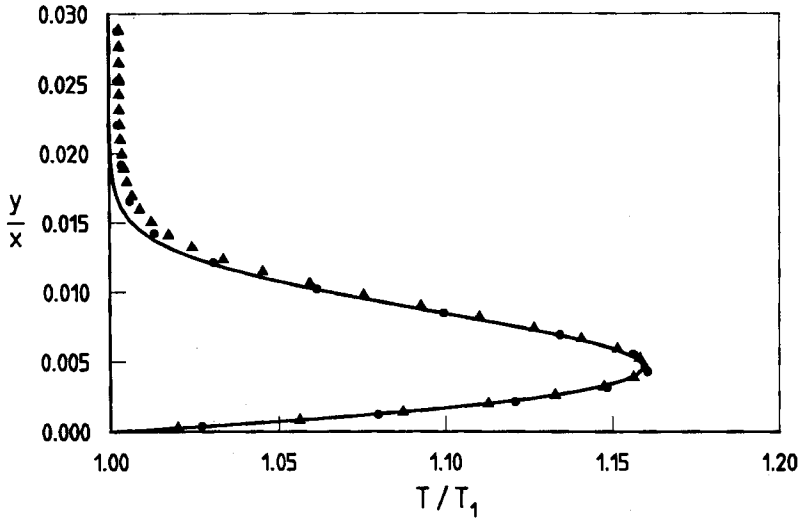

Figure 10. EIM compared with other methods: —— spectral method of Reference 17; ●, finite volume method of Reference 15; ▲, EIM. Temperature profile at $x/L=0{\cdot}916$, $tU_1/L=4{\cdot}78$. EIM on grid 3, Table I.

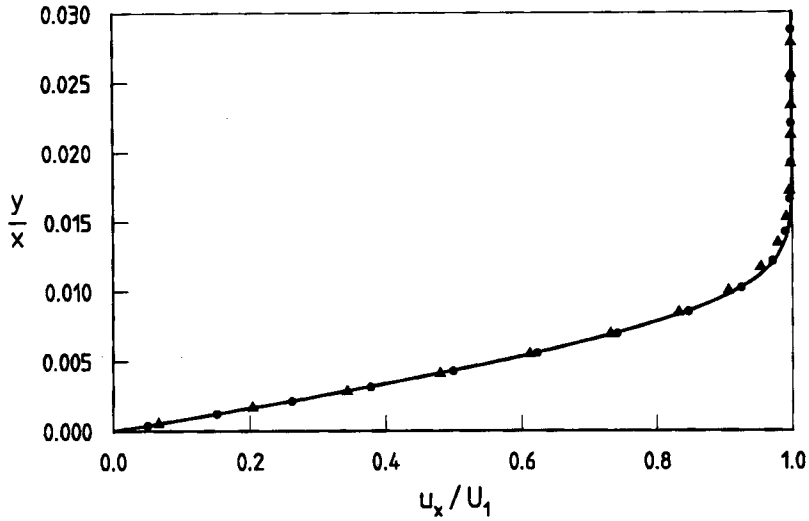

Figure 11. Velocity profile at $x/L=0{\cdot}916$, $tU_1/L=4{\cdot}78$. EIM on grid 1, Table I. See Figure 10 for legend

Jacobs' results, the total processing time was 1·6 h on a single processor of a Cray Y-MP. The total CPU time for the EIM calculation of Figure 10 was 10·0 h on a SUN Microsystems SPARC station 2 which, taking the speed of this machine as 1/30 of the Cray Y-MP, compares very favourably with the conventional method. For the grid used to obtain the results in Figure 11 the total CPU time was only 2·74 h on the SPARC station.

There are a number of reasons for this decrease in computational effort (for a comparable degree of accuracy) for EIM. One reason is that EIM requires no iteration to determine the

interface states, as is required with the Riemann solver in the conventional method. No calculation of flow gradients within cells has been used in EIM and this also accounts for some decrease in the computational effort. Another reason may be that, because of the regular grid used in these computations, the calculation of the gradients required in the determination of the dissipative fluxes is less expensive than for a non-orthogonal grid. The principal reason for the small computational effort required, however, is the good accuracy of EIM for large cell sizes. This is discussed further below.

8. CONCLUSIONS

A new kinetic-theory-based numerical method has been shown to produce accurate solutions of the Navier–Stokes equations for two flows containing strong gradients: the interior region of a plane shock, and the boundary layer on a flat plate. The plane shock calculations showed that the new method was able to produce accurate results for cell sizes large relative to the flow structure being resolved. The boundary layer calculations with the new method showed that it produced solutions of accuracy comparable to those of another finite volume method which uses a Riemann solver and a spatially second-order-accurate estimation of flow states within cells. The new method required considerably less computational effort.

The principal reason for the reduced computational effort is the accuracy of the kinetic method which allows the use of relatively large cells. The computational expense of an explicit time step method arises from the small time step which must be used to keep the CFL number small in all the cells. Because of the very small cells used by Jacobs, his method required an order of magnitude greater number of time steps than did ours. Some of our advantage was lost since we used more (though generally not smaller) cells. We have not yet applied the method on a skewed or highly stretched grid, which would enable far fewer cells to be used, but we would expect a further reduction in computational time for a similar accuracy.

For flows containing strong shocks, an accurate solution of the Navier–Stokes equations throughout the flow, including the interior of shocks, would be expected to produce shock thicknesses which are orders of magnitude less than the cell size in any feasible grid. The calculations for the internal structure of the plane shock did raise the question as to whether EIM would remain stable when the cell size became very large compared to the shock thickness. For the flat-plate boundary layer, a weak shock spread over many cells is captured by EIM, which is encouraging, but as it stands, EIM can be considered only as a first step towards a general robust and accurate kinetic theory solution method for the Navier–Stokes equations. To make EIM robust without losing accuracy, more dissipation might be added where discontinuities form, but not elsewhere. One possibility is to blend the fluxes from EIM and a more dissipative method with a weighting which is varied by some sort of switching like that used in Jameson's Euler solver[18] to vary the artificial viscosity. Natural choices for the more dissipative fluxes which may be required are the dissipative components of the fluxes in Pullin's kinetic theory EFM, which are given by (29)–(35). This possibility is not explored further here.

ACKNOWLEDGEMENT

This work was supported by the Australian Research Council under grant number A 89031403.

REFERENCES

1. D. I. Pullin, 'Direct simulation methods for compressible ideal-gas flow', *J. Comput. Phys.*, **34**, 231–244 (1980).
2. R. D. Reitz, 'One-dimensional compressible gas dynamics calculations using the Boltzmann equation', *J. Comput. Phys.*, **42**, 108–123 (1981).

3. S. M. Deshpande, 'Kinetic theory based new upwind methods for inviscid compressible flows', *AIAA Paper 86-0275*, 1986.
4. M. N. Macrossan, 'The equilibrium flux method for the calculation of flows with non-equilibrium chemical reactions', *J. Comput. Phys.*, **80**, 204–231 (1989).
5. M. N. Macrossan, 'Hypervelocity flow of dissociating nitrogen downstream of a blunt nose', *J. Fluid Mech.*, **207**, 167–202 (1990).
6. M. N. Macrossan, D. I. Pullin and N. J. Richter, 'Calculations of a three-dimensional hypervelocity cone-flow with chemical reactions', *Proc. 10th Australian Fluid Mechanics Conf.*, Vol. 2, paper 12.33, 1989.
7. M. N. Macrossan and D. I. Pullin, 'Hypervelocity cone-flow with reaction chemistry by second order kinetic theory based Euler solver', *Proc. 3rd Australian Supercomp. Conf.*, paper 12-C, 1989.
8. B. van Leer, 'Towards the ultimate conservation difference scheme', *J. Comput. Phys.*, **32**, 101–136 (1979).
9. H. C. Yee, 'A class of high-resolution explicit and implicit shock-capturing methods', *NASA TM-101088*, 1989.
10. S. Chapman and T. G. Cowling, *The Mathematical Theory of Non-uniform Gases*, CUP, 1952.
11. P. L. Roe, 'Approximate Riemann solvers, parameter vectors and difference schemes', *J. Comput. Phys.*, **43**, 357–372 (1981).
12. R. I. Oliver, 'A kinetic theory method for the Navier–Stokes equations', *Bachelor of Engineering Thesis*, Department of Mechanical Engineering, University of Queensland, 1990.
13. D. Gilbarg and D. Paolucci, 'The structure of shock waves in the continuum theory of fluids', *J. Rat. Mech. Anal.*, **2**, 617–642 (1953).
14. C. Truesdell, 'Precise theory of the absorption and dispersion of forced plane infinitesimal waves according to the Navier–Stokes equations', *J. Rat. Mech. Anal.*, **2**, 643–743 (1953).
15. P. A.. Jacobs, 'Single-block Navier–Stokes integrator', *NASA CR-187613, ICASE interim Report 18*, July 1991.
16. P. A. Jacobs, 'Approximate Riemann solver for hypervelocity flows', *AIAA J*, **30**, 2555–2561 (1992).
17. C. D. Pruett and C. L. Street, 'A spectral collocation method for compressible, nonsimilar boundary layers', *Int. j. numer. methods fluids*, **13**, 713–737 (1991).
18. A. Jameson, W. Schmidt and E. Turkel, 'Numerical solutions of the Euler equations by finite volume methods using Runge–Kutta time stepping schemes', *AIAA Paper 81-1259*, 1981.